

Variational Quantum Simulation of Valence-Bond Solids

Daniel Huerga^{1,2,*}

¹Quantum Matter Institute, University of British Columbia, Vancouver, BC, Canada V6T 1Z4

²Department of Physical Chemistry, University of the Basque Country UPV/EHU, Apartado 644, 48080 Bilbao, Spain

(Dated: May 9, 2022)

We introduce a hybrid quantum-classical variational algorithm to simulate ground-state phase diagrams of frustrated quantum spin models in the thermodynamic limit. The method is based on a cluster-Gutzwiller ansatz where the wave function of the cluster is provided by a parameterized quantum circuit whose key ingredient is a two-qubit real XY gate allowing to efficiently generate valence-bonds on nearest-neighbor qubits. Additional tunable single-qubit Z- and two-qubit ZZ-rotation gates allow the description of magnetically ordered and paramagnetic phases while restricting the variational optimization to the U(1) subspace. We benchmark the method against the J_1 - J_2 Heisenberg model on the square lattice and uncover its phase diagram, which hosts long-range ordered Néel and columnar anti-ferromagnetic phases, as well as an intermediate valence-bond solid phase characterized by a periodic pattern of 2×2 strongly-correlated plaquettes. Our results show that the convergence of the algorithm is guided by the onset of long-range order, opening a promising route to synthetically realize frustrated quantum magnets and their quantum phase transition to paramagnetic valence-bond solids with currently developed superconducting circuit devices.

Hybrid quantum-classical variational algorithms, so-called variational quantum algorithms (VQA), are at the center of current research for their potentialities in providing *useful* applications of currently developed noisy intermediate scale quantum (NISQ) devices [1]. They consist in a generic feedback loop where the NISQ device provides a quantum state via a parameterized quantum circuit (PQC) that is tuned by a classical computer so as to optimize a certain objective function encoding the problem of interest [2–4]. The variational quantum eigensolver [5] was one of the first VQA proposed to approximate the ground-state and energy of *finite* strongly-correlated fermionic Hamiltonians as an alternative to the phase estimation algorithm [6], which provides the exact ground-state solution but requires coherence times on the quantum devices unreachable with current technology.

The initially expected unleashed potentialities of VQA towards providing quantum advantage on problems including machine learning, optimization, and the simulation of strongly-correlated electron systems—a foundational motivation driving research in quantum computation [7–13]—have been narrowed down due to the identification of various limitations. Specifically, the optimization landscape has been shown to be plagued with so-called *barren plateaux* [14], large flat regions hindering optimization that may appear independently of the optimization routine used [15]. Additionally, suboptimal minima have been argued to render the classical optimization problem NP-hard [16]. In spite of these limitations, *local* objective functions, e.g. the energy of a local Hamiltonian, may still be efficiently optimized for shallow PQCs in certain regimes [17].

In particular, two-dimensional (2D) frustrated quantum magnets, characterized by the impossibility of finding a spin arrangement satisfying all local energy constraints simultaneously in any locally-rotated basis [18], provide a

natural testbed arena for VQAs and NISQ devices. They pose a challenge to state-of-the-art classical numerical methods [19–21] and at the same time host a plethora of phases and phenomena of both fundamental and applied interest. In particular, quantum paramagnetic phases either breaking or preserving translational symmetry—so-called valence-bond solids (VBS) and quantum spin-liquids (QSL), respectively—, have important implications for layered materials [22–24] and quantum computation [25–29]. Recent developed hybrid approaches have mainly focused on the simulation of 1D lattices [30–34], while approaches to 2D have been more scarce and limited to finite systems [34, 35].

In this work, we introduce a cluster-Gutzwiller VQA to simulate ground-state phase diagrams of frustrated 2D quantum spin models *in the thermodynamic limit*. We build upon the grounds of hierarchical mean-field theory (HMFT) [36], an algebraic framework based on the use of clusters for which a Gutzwiller ansatz represents the lowest order approximation. Furnished with a scaling analysis, it allows to uncover ground-state phase diagrams in the thermodynamic limit characterized by co-existence and competition of different long-range orders (LROs) and quantum paramagnetic phases [37–42]. Aiming at overcoming the scaling limitations of HMFT, we present its *quantum-assisted* approach, dubbed Q-HMFT, where the cluster wave function is generated via a PQC whose central element is a parameterized real two-qubit XY gate that efficiently generates valence-bonds on nearest-neighbor (NN) qubits. Respecting the squared connectivities of currently developed chips [43, 44], we provide a systematic PQC construction resulting in shallower depths than other commonly used PQC ansätze, which either admix symmetry sectors [45, 46] or require higher chip connectivities [11]. Information about the thermodynamic limit is implemented at the objective function level (i.e. the

energy) through the self-consistent mean-field embedding concomitant to the cluster-Gutzwiller ansatz. Such mean-field embedding pushes the convergence of Q-HMFT away from barren-plateaux within LRO phases, while paramagnetic phases are accessed by smoothly tuning the system through a quantum phase transition. We benchmark numerically Q-HMFT on the paradigmatic antiferromagnetic J_1 - J_2 model on the square lattice [47, 48], which hosts Néel and columnar anti-ferromagnet (CAF) LROs, as well as a long-dubeted intermediate paramagnetic phase [39, 49–62]. Consistently with previous classical results from HMFT [39] and other state-of-the-art algorithms [51, 52, 56, 59], we find that the Néel melts onto a VBS characterized by a 2×2 *plaquette* ordering. Convergence results from up to a 4×4 -qubit cluster suggest the potential scalability of Q-HMFT, making it a promising route to quantum simulate frustrated magnets and valence-bond solid phases with currently developed superconducting qubit devices beyond classical capabilities.

Quantum-assisted hierarchical mean-field.—Let us consider a generic translational invariant 2-body local Hamiltonian in the infinite lattice, $H = \sum_{i,j} h_{i,j}$, where $h_{i,j} = J_{i,j} \mathbf{S}_i \mathbf{S}_j$ and $\mathbf{S}_i = (S_i^x, S_i^y, S_i^z)$ refers to the $S=1/2$ SU(2) spin operators at site i , and $J_{i,j}$ to the two-spin interaction strength. We tile the lattice with N -site equivalent clusters preserving as much as possible the original symmetries of the lattice. We classify the Hamiltonian terms on those acting within clusters, $h_R^\square = \sum_{(i,j) \in R} h_{i,j}$, and those acting on two different clusters, $h_{R,R'}^I = \sum_{i \in R, j \in R'} h_{i,j}$, where R labels the position of the cluster in the tiled lattice, or superlattice. We define a uniform cluster-Gutzwiller ansatz as the product state of N -site clusters in the infinite lattice,

$$|\Psi(\boldsymbol{\theta})\rangle = \bigotimes_R |\psi(\boldsymbol{\theta})\rangle, \quad (1)$$

where we have restricted all clusters R to be in a same normalized state, $|\psi(\boldsymbol{\theta})\rangle$, parameterized by $\boldsymbol{\theta} = \{\theta_k\}$. Considering the wave function (1), the energy per spin reduces to the contribution of a single cluster and its mean-field embedding [39–41],

$$E(\boldsymbol{\theta}) = \frac{1}{N} \left(\langle h^\square \rangle_{\boldsymbol{\theta}} + \frac{1}{2} \sum_{i \in \square, j \in \square'} J_{i,j} \langle \mathbf{S}_i \rangle_{\boldsymbol{\theta}} \langle \mathbf{S}_j \rangle_{\boldsymbol{\theta}} \right), \quad (2)$$

where $\langle \cdot \rangle_{\boldsymbol{\theta}}$ refers to the expectation value with the parameterized cluster wave function (1). The first summand in (2) accounts for the intra-cluster contributions, while the second runs over all two-spin inter-cluster interactions with the neighboring clusters, \square' (the $1/2$ preventing double counting) and provides information about the thermodynamic limit by allowing the breakdown of symmetries and concomitant onset of LROs. Generalization to n -body interactions appearing in e.g. ring-exchange models is straightforward [37, 41, 63]. The optimal energy $E = E(\boldsymbol{\theta}^*)$

with parameters $\boldsymbol{\theta}^*$ is obtained upon minimization of the variational energy (2). Generically, the exact limit is recovered at $N \rightarrow \infty$. Thus, by increasing the cluster size, we assess the stability of the phase diagram. However, exact diagonalization of the clusters is typically limited to $N \lesssim 30$ with classical computing means, which conforms the major bottleneck of the method [38–40, 42, 63].

In order to overcome such limitation, here we consider a PQC generating the cluster wave function,

$$|\psi(\boldsymbol{\theta})\rangle = \mathcal{U}(\boldsymbol{\theta}) |\psi_0\rangle, \quad (3)$$

where $|\psi_0\rangle$ is an initial easy-to-prepare state, here onwards fixed to $|\psi_0\rangle = |0101\dots 01\rangle$ for reasons that will be clear below, with $|0\rangle \doteq |\uparrow\rangle$, $|1\rangle \doteq |\downarrow\rangle$, and $\mathcal{U}(\boldsymbol{\theta})$ a digitalized unitary transformation, $\mathcal{U}(\boldsymbol{\theta}) = \prod_k U_k(\theta_k)$ where $U_k(\theta_k) = e^{-i\theta_k V_k}$ with V_k an hermitian operator acting on either one or two qubits.

For SU(2) Hamiltonians on a bipartite lattice, we may restrict the variational search to the U(1) subspace of null total magnetization, $\sum_{j \in \square} \langle S_j^z \rangle = 0$. Within the two-qubit $S^z=0$ subspace, spanned by $|\tilde{0}\rangle \doteq |10\rangle$ and $|\tilde{1}\rangle \doteq |01\rangle$, any transformation can be generated by the XY-Heisenberg, $\tilde{S}_{ij}^x = (S_i^x S_j^x + S_i^y S_j^y)$, and the z -projection of the Dzialoshinskii-Moriya (DM), $\tilde{S}_{ij}^y = (S_i^x S_j^y - S_i^y S_j^x)$, interactions. Together with $\tilde{S}_{ij}^z = \frac{1}{2}(S_j^z - S_i^z)$, they form a SU(2) algebra, $[\tilde{S}_{ij}^\alpha, \tilde{S}_{ij}^\beta] = i\epsilon^{\alpha\beta\gamma} \tilde{S}_{ij}^\gamma$. In particular, a rotation generated by the DM interaction, $V_{ij} = \tilde{S}_{ij}^y$, leads to a purely real XY-gate,

$$U_{ij}^{\text{XY}}(\theta) = \cos(\theta/2)(|01\rangle\langle 01| + |10\rangle\langle 10|) + \sin(\theta/2)(|01\rangle\langle 10| - |10\rangle\langle 01|), \quad (4)$$

which efficiently transforms an uncorrelated Néel into a singlet, i.e. a *valence-bond*, $U_{ij}^{\text{XY}}(\frac{\pi}{2}) |01\rangle_{ij} = \frac{1}{\sqrt{2}}(|01\rangle_{ij} - |10\rangle_{ij})$. The REAL-XY gate (4) can be considered as a generalization of a Givens rotations [64], and its use has been proposed for the digital preparation of fermionic Slater determinants [12, 13]. Recently, a controlled version of it has been argued to be universal [65]. From the experimental standpoint, recent implementations have shown fidelities $\sim 97\%$ [66].

Considering the square connectivities of currently developed superconducting quantum chips [43, 44], we use $L \times L$ qubit clusters with even L . We construct the PQC (3) by applying REAL-XY gates (4) to all pairs of NN qubits in an order that (i) minimizes the total depth of the PQC and (ii) favors the C_4 symmetry of the square lattice. We increase the amount of correlations by adding a set of parameterized ZZ-rotations, $U_{ij}^{\text{ZZ}}(\theta) = e^{-i\theta Z_i Z_j}$ where $Z_j = 2S_j^z$, and a final layer of single-qubit parameterized Z-rotation gates, $U_j^Z(\theta) = e^{-i\theta Z_j}$, both of them realizable experimentally [67]. Such a XY-ZZ-Z macro-layer is recursively applied a few times m to improve accuracy.

Specifically,

$$\mathcal{U} = \prod_m \left(\mathcal{U}^Z \prod_{g=XY,ZZ} [T_y \mathcal{U}_y^g] [T_x \mathcal{U}_x^g] \mathcal{U}_y^g \mathcal{U}_x^g \right), \quad (5)$$

where we have defined $\mathcal{U}_\alpha^g = \prod_k U_{(\mathbf{r}_k, \mathbf{r}_k + \hat{e}_\alpha)}^g(\theta_k^m)$ as the product of g -type two-qubit gates applied to NN dimers in a columnar pattern along $\alpha = \{x, y\}$, where $\mathbf{r}_k = (x_k, y_k)$ labels the position of the qubit considering the bottom-left corner as the origin, and \hat{e}_α is the unit vector. That is, $0 \leq x_k \leq L - 2$ (for even x_k) and $0 \leq y_k \leq L - 1$ for \mathcal{U}_x^g , and vice versa for \mathcal{U}_y^g . The operator $T_\alpha \mathcal{U}_\alpha^g$ refers to the translation of \mathcal{U}_α^g by \hat{e}_α , and $\mathcal{U}^Z = \prod_j U_{\mathbf{r}_j}^Z(\theta_j)$ is the last single-qubit layer. For $L=2$, no translation operators are needed to uncover all NNs, thus $d=5m$. For $L \geq 4$, the PQC (5) has $n=(5L^2 - 4L)m$ variational parameters and a depth $d=9m$ independent of the number of qubits (see Supplementary Material). As shown in the following, a small $m=2$ is sufficient to provide with a good approximation to HMFT.

Numerical results.—We benchmark Q-HMFT on the antiferromagnetic J_1 - J_2 Heisenberg model on the square lattice [47, 48],

$$H = J_1 \sum_{\langle i,j \rangle} \mathbf{S}_i \mathbf{S}_j + J_2 \sum_{\langle\langle i,j \rangle\rangle} \mathbf{S}_i \mathbf{S}_j, \quad (6)$$

where $\langle i,j \rangle$ and $\langle\langle i,j \rangle\rangle$ account for NN and next-to-NN pairs of sites, respectively. From here onwards, we express all quantities in units of J_1 . Upon tuning $J_2 > 0$, model (6) hosts Néel and CAF ordered phases, and an intermediate quantum paramagnetic phase in between that is a matter of debate [39, 49–62]. Proposals have fluctuated through the time, including different QSLs [55, 57, 58], and VBSs with a pattern of *dimers* [49, 50, 60] or 2×2 *plaquettes* [51, 56, 59] breaking or preserving C_4 symmetry, respectively, the last scenario being described by HMFT [39]. Interestingly, upon introducing third-NN Heisenberg interaction, the plaquette-VBS order becomes stronger [52] and has been argued to be of a higher-order symmetry-protected topological type [68].

We perform ideal noiseless classical simulations of Q-HMFT on the J_1 - J_2 model (6) with 2×2 and 4×4 clusters, and $m=2$ and 4 macro-layers. We compute energy, magnetization and dimer observables, as well as provide details on its convergence, and compare with the classical HMFT results with the same clusters, which provide with a satisfactory extrapolation to the $N \rightarrow \infty$ limit, $E_\infty(J_2 = 0) \simeq -0.64$ [39], when compared to that obtained with state-of-the-art computational techniques, $E_\infty(J_2 = 0) \simeq -0.67$ [54, 69]. As a classical optimizer, we use the gradient-based L-BFGS-B algorithm [70, 71], where the gradient of the energy is computed via two-point first order approximation, $\partial_{\theta_k} E = (E_{\theta_k + \delta} - E_{\theta_k}) / |\delta|$, for $\delta = 10^{-10}$ along k direction in variational space. We uncover the phase diagram by first obtaining an optimal

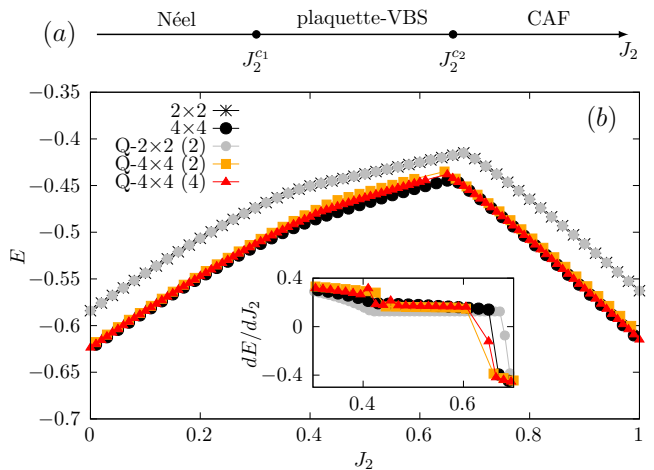


FIG. 1. (a) Schematic phase diagram of the J_1 - J_2 model (6) as computed with hybrid and classical versions of HMFT- $L \times L$. (b) Energy per spin (2) and first derivative (inset) computed with Q-HMFT- $L \times L$ and m macro-layers, labeled Q- $L \times L$ (m), together with HMFT results (labeled $L \times L$) for $L=2, 4$, and $m=2, 4$.

solution from various random PQC initializations at each extreme (i.e. $J_2=0$ and $J_2=1$), and then smoothly tuning the Hamiltonian parameters. We compute the energy (2) and its derivatives to detect quantum phase transitions, as well as magnetic and dimer orders to characterize the phases.

In Fig. 1, we show the optimal energy per spin and first derivative with respect to J_2 as computed with Q-HMFT with $m=2$ and $m=4$ macro-layers, together with HMFT results. For 2×2 clusters, Q-HMFT with $m=2$ and equal parameters within XY and ZZ layers, respectively (i.e. 12 variational parameters), provides an *exact* hybrid realization of HMFT, describing a Néel phase and its melting through second order quantum phase transition onto a plaquette-VBS at $J_2^{c1} \simeq 0.42$, and a posterior first order phase transition at $J_2^{c2} \simeq 0.68$. For 4×4 , Q-HMFT provides an excellent approximation to HMFT, increasing its accuracy as we increase the number of macro-layers. Specifically, it shows a weak first order transition at $J_2^{c1} \simeq 0.44$ that tends towards second order upon increasing m , while the transition point moves towards the one obtained by HMFT, $J_2^{c1} \simeq 0.42$. At $J_2^{c2} \simeq 0.64$, it shows a clear first order transition, which moves to the HMFT result, $J_2^{c2} \simeq 0.66$, upon increasing m .

To characterize the phases, first we inspect the magnetization,

$$M^z(\mathbf{k}) = \frac{1}{N} \sum_j e^{-i\mathbf{r}_j \mathbf{k}} \langle S_j^z \rangle, \quad (7)$$

where $\mathbf{r}_i = (r_i^x, r_i^y)$ refers to the position of site i in the infinite lattice and \mathbf{k} to a vector in the first Brillouin zone. Néel and CAF LROs are signaled by finite $M^z(\pi, \pi)$ and

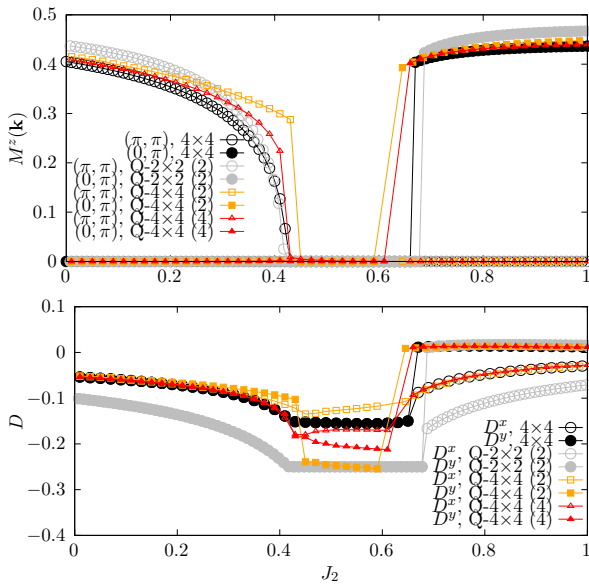


FIG. 2. Top: Néel (empty points) and CAF (filled points) LRO parameters computed with Q-HMFT- $L \times L$ and m (labeled Q- $L \times L$ (m)), and HMFT results (labeled $L \times L$). Bottom: Dimer observable along x (empty points) and y (filled points) with Q- and HMFT.

$M^z(0, \pi)$ (equivalently, $M^z(\pi, 0)$), respectively. In Fig. (2) (top) we show Q-HMFT results on the magnetization together with HMFT- 4×4 for comparison. For 2×2 clusters, Q-HMFT ($m=2$) reproduces exactly HMFT results (not shown for clarity purposes) showing the continuous vanishing of the Néel order parameter, an intermediate paramagnetic region, and a following discontinuous onset of CAF order, consistent with the description of second and first order phase transitions, respectively. For 4×4 clusters, Q-HMFT tends towards HMFT results upon increasing m , essentially providing the same phase diagram as with (Q-)HMFT- 2×2 . In particular, the vanishing of the Néel order parameter is discontinuous with $m=2$ (consistent with the first order transition seen in the energy), but such discontinuity decreases upon increasing $m=4$, suggesting a continuous vanishing for $m>4$ as found with HMFT.

In order to characterize the possible onset of VBS order in the intermediate paramagnetic phase, we define the dimer observable along $\alpha = x, y$ allowing to distinguish between dimer or plaquette order [51],

$$D^\alpha = \frac{1}{L} \sum_{\langle i, j \rangle_\alpha} (-1)^{r_i^\alpha} \langle \mathbf{S}_i \mathbf{S}_j \rangle, \quad (8)$$

where $\langle i, j \rangle_\alpha$ refers to nearest-neighbor bonds along α . Specifically, $D^x \neq D^y$ signals the onset of dimer-VBS along one direction, while $D^x = D^y$ provides a signature of a C_4 preserving plaquette-VBS. In Fig. (2) (bottom) we show dimerization for Q-HMFT and its classical counterpart. For 2×2 , Q-HMFT reproduces exactly HMFT results (not

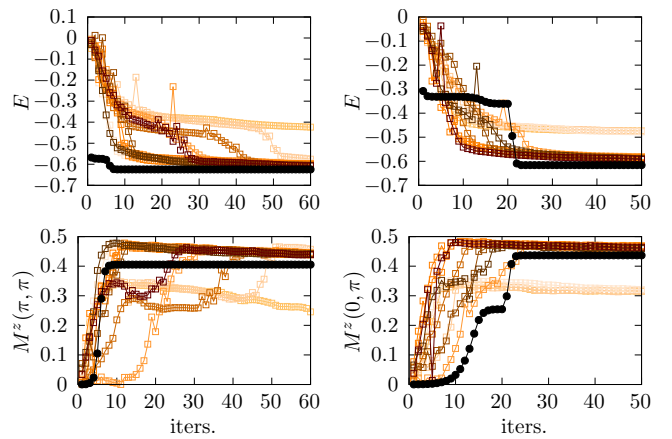


FIG. 3. Convergence of energy and order parameters for $J_2=0$ (left) and $J_2=1$ (right) with Q-HMFT- 4×4 , $m=2$, from 10 random initializations of the PQC (empty squares, orange scale) together with HMFT- 4×4 (black dots) from a random initialization.

shown for clarity purposes) showing a non-zero $D^x = D^y$ within the Néel phase that increases in absolute value and reaches a plateau indicating the plaquette-VBS at J_2^{c1} . Upon further tuning J_2 , both dimer observables show a discontinuity at J_2^{c2} consistent with the first order transition found upon inspecting the energy, after which $D_y \simeq 0$ and $D_x < 0$ consistent with CAF ordering along y . For 4×4 clusters, HMFT essentially provides the same picture, but with a reduced value of the dimerization throughout the phase diagram. Q-HMFT approximates quantitatively well HMFT results within the LRO phases, but shows a slight breakdown of the C_4 symmetry (i.e. $D_y < D_x$) within the intermediate plaquette-VBS. Nevertheless, such difference is reduced upon increasing m , tending towards the HMFT- 4×4 results.

Last, we analyze the scalability of Q-HMFT by computing the variance of the first component of the energy gradient, $\text{Var}[\partial_{\theta_1} E_\theta]$, and inspecting the convergence of the algorithm. Although the variance computed with Q-HMFT ($m=2$) shows a strong suppression with increasing cluster size, specifically $\text{Var}(N=4) \sim O(1)$ and $\text{Var}(N=16) \sim O(10^{-2})$, the convergence of Q-HMFT within LRO phases is pushed by the mean-fields concomitant to the onset of LRO, as can be seen in Fig. 3 for Q-HMFT- 4×4 ($m=2$) at $J_2=0$ (Néel) and $J_2=1$ (CAF) for 10 random initializations of the PQC. The system may explore suboptimal minima, but in most of the cases some extra tens of iterations permit the system to escape from them and approximate the HMFT result.

Conclusion and outlook.—We have presented a hybrid algorithm to quantum simulate 2D quantum frustrated magnets in infinite lattices. Based on the cluster-Gutzwiller ansatz, we present a quantum-assisted approach to HMFT [39–42], dubbed Q-HMFT, where the wave function of a finite cluster is provided by a $U(1)$

symmetry preserving PQC that respects the native NN square connectivities of currently developed superconducting quantum circuits. The thermodynamic limit is accounted for by a self-consistent mean-field embedding introduced at the objective function level, i.e. the energy. Such mean-field embedding guides the convergence of the algorithm away from potential barren-plateaux within the ordered phases. The main ingredient of the PQC is a parameterized REAL-XY gate performing generalized Givens rotations in the two-qubit odd-parity subspace and efficiently generating valence-bonds. Further addition of parameterized ZZ- and Z-rotations furnish a fixed-depth macro-layer for general even $L \times L$ -qubit clusters. Benchmark numerical results on the paradigmatic frustrated J_1 - J_2 Heisenberg model on the square lattice with 2×2 and 4×4 clusters show that just two macro-layers are sufficient to approach previous HMFT results [39] describing a phase diagram with Néel and columnar antiferromagnetic orders, as well as an intermediate quantum paramagnetic *plaquette*-VBS phase, in accordance with results from state-of-the-art classical numerical techniques [51, 52, 59]. The VBS is accessed by smoothly tuning the system across the Néel to VBS quantum phase transition to avoid eventual barren-plateaux. These results suggest the potential scalability of Q-HMFT to large cluster sizes inaccessible by classical HMFT, i.e. even $L > 4$, whose simulation would require highly involved classical algorithms [72–75], and ultimately, purely quantum computing means. Q-HMFT may be implemented with other technologies, in particular those hosting native XY gates [31] capable to realize different 2D lattices [76]. Moreover, the simulation of 2D Hamiltonians hosting *exact* VBS ground-states [63, 77] via Q-HMFT offers a means for benchmarking quantum devices [78]. In addition, the symmetry-guided construction of the PQC makes it suitable for developing error mitigation strategies [79], or the description of low-energy excitations over the ground-state [40, 80]. From the experimental standpoint, we expect these results to motivate further development and refinement of the family of parameterized XY gates [81–83] as key elements for variational quantum algorithms.

We acknowledge useful discussions with Adrián Parra-Rodríguez, Alberto Nocera, Polina Feldmann, Christopher Eichler, Gerardo Ortiz, and Robert Raussendorf. We gratefully acknowledge G. Ortiz for providing access to computing facilities of the Department of Physics, Indiana University. This research has been funded by the Canada First Research Excellence Fund, Quantum Materials and Future Technologies Program, and the OpenSuperQ project (grant agreement 820363) of the EU Quantum Flagship program.

* daniel.huerga@ubc.ca

- [1] J. Preskill, Quantum Computing in the NISQ era and beyond, *Quantum* **2**, 79 (2018).
- [2] J. R. McClean, J. Romero, R. Babbush, and A. Aspuru-Guzik, The theory of variational hybrid quantum-classical algorithms, *New Journal of Physics* **18**, 023023 (2016).
- [3] M. Cerezo, A. Arrasmith, R. Babbush, S. C. Benjamin, S. Endo, K. Fujii, J. R. McClean, K. Mitarai, X. Yuan, L. Cincio, *et al.*, Variational quantum algorithms, *Nat. Rev. Phys.* **3**, 625 (2021).
- [4] K. Bharti, A. Cervera-Lierta, T. H. Kyaw, T. Haug, S. Alperin-Lea, A. Anand, M. Degroote, H. Heimonen, J. S. Kottmann, T. Menke, *et al.*, Noisy intermediate-scale quantum algorithms, *Rev. Mod. Phys.* **94**, 015004 (2022).
- [5] A. Peruzzo, J. McClean, P. Shadbolt, M.-H. Yung, X.-Q. Zhou, P. J. Love, A. Aspuru-Guzik, and J. L. O’Brien, A variational eigenvalue solver on a photonic quantum processor, *Nat. Commun.* **5**, 4213 (2014).
- [6] M. A. Nielsen and I. L. Chuang, *Quantum Computation and Quantum Information: 10th Anniversary Edition* (Cambridge University Press, 2010).
- [7] R. P. Feynman, Simulating physics with computers, *Int. J. Theor. Phys.* **21**, 467 (1982).
- [8] D. S. Abrams and S. Lloyd, Simulation of many-body Fermi systems on a universal quantum computer, *Phys. Rev. Lett.* **79**, 2586 (1997).
- [9] G. Ortiz, J. E. Gubernatis, E. Knill, and R. Laflamme, Quantum algorithms for fermionic simulations, *Phys. Rev. A* **64**, 022319 (2001).
- [10] R. Somma, G. Ortiz, J. E. Gubernatis, E. Knill, and R. Laflamme, Simulating physical phenomena by quantum networks, *Phys. Rev. A* **65**, 042323 (2002).
- [11] D. Wecker, M. B. Hastings, and M. Troyer, Progress towards practical quantum variational algorithms, *Phys. Rev. A* **92**, 042303 (2015).
- [12] D. Wecker, M. B. Hastings, N. Wiebe, B. K. Clark, C. Nayak, and M. Troyer, Solving strongly correlated electron models on a quantum computer, *Phys. Rev. A* **92**, 062318 (2015).
- [13] Z. Jiang, K. J. Sung, K. Kechedzhi, V. N. Smelyanskiy, and S. Boixo, Quantum algorithms to simulate many-body physics of correlated fermions, *Phys. Rev. Applied* **9**, 044036 (2018).
- [14] J. R. McClean, S. Boixo, V. N. Smelyanskiy, R. Babbush, and H. Neven, Barren plateaus in quantum neural network training landscapes, *Nat. Commun.* **9**, 4812 (2018).
- [15] A. Arrasmith, M. Cerezo, P. Czarnik, L. Cincio, and P. J. Coles, Effect of barren plateaus on gradient-free optimization, *Quantum* **5**, 558 (2021).
- [16] L. Bittel and M. Kliesch, Training variational quantum algorithms is NP-hard, *Phys. Rev. Lett.* **127**, 120502 (2021).
- [17] M. Cerezo, A. Sone, T. Volkoff, L. Cincio, and P. J. Coles, Cost function dependent barren plateaus in shallow parametrized quantum circuits, *Nat. Commun.* **12**, 1791 (2021).
- [18] C. Lacroix, P. Mendels, and F. Mila, *Introduction to Frustrated Magnetism: Materials, Experiments, Theory*, Springer Series in Solid-State Sciences (Springer Berlin Heidelberg, 2011).
- [19] N. Hatano and M. Suzuki, Representation basis in quantum Monte Carlo calculations and the negative-sign problem, *Phys. Lett. A* **163**, 246 (1992).
- [20] M. Troyer and U.-J. Wiese, Computational complexity and fundamental limitations to fermionic quantum Monte

- Carlo simulations, *Phys. Rev. Lett.* **94**, 170201 (2005).
- [21] M. Marvian, D. A. Lidar, and I. Hen, On the computational complexity of curing non-stoquastic Hamiltonians, *Nat. Commun.* **10**, 1571 (2019).
- [22] M. R. Norman, Colloquium: Herbertsmithite and the search for the quantum spin liquid, *Rev. Mod. Phys.* **88**, 041002 (2016).
- [23] M. E. Zayed, C. Rüegg, J. Larrea J., A. M. Läuchli, C. Panagopoulos, S. S. Saxena, M. Ellerby, D. F. McMorrow, T. Strässle, S. Klotz, *et al.*, 4-spin plaquette singlet state in the Shastry–Sutherland compound $\text{SrCu}_2(\text{BO}_3)_2$, *Nat. Phys.* **13**, 962 (2017).
- [24] Y. Zhou, K. Kanoda, and T.-K. Ng, Quantum spin liquid states, *Rev. Mod. Phys.* **89**, 025003 (2017).
- [25] F. Verstraete and J. I. Cirac, Valence-bond states for quantum computation, *Phys. Rev. A* **70**, 060302(R) (2004).
- [26] T.-C. Wei, I. Affleck, and R. Raussendorf, Affleck-Kennedy-Lieb-Tasaki state on a honeycomb lattice is a universal quantum computational resource, *Phys. Rev. Lett.* **106**, 070501 (2011).
- [27] A. Miyake, Quantum computational capability of a 2D valence bond solid phase, *Ann. Phys.* **326**, 1656 (2011).
- [28] A. Kitaev, Fault-tolerant quantum computation by anyons, *Ann. Phys.* **303**, 2 (2003).
- [29] A. Kitaev, Anyons in an exactly solved model and beyond, *Ann. Phys.* **321**, 2 (2006).
- [30] C. Schön, E. Solano, F. Verstraete, J. I. Cirac, and M. M. Wolf, Sequential generation of entangled multiqubit states, *Phys. Rev. Lett.* **95**, 110503 (2005).
- [31] C. Kokail, C. Maier, R. van Bijnen, T. Brydges, M. K. Joshi, P. Jurcevic, C. A. Muschik, P. Silvi, R. Blatt, C. F. Roos, and P. Zoller, Self-verifying variational quantum simulation of lattice models, *Nature* **569**, 355 (2019).
- [32] M. Foss-Feig, D. Hayes, J. M. Dreiling, C. Figgatt, J. P. Gaebler, S. A. Moses, J. M. Pino, and A. C. Potter, Holographic quantum algorithms for simulating correlated spin systems, *Phys. Rev. Research* **3**, 033002 (2021).
- [33] F. Barratt, J. Dborin, M. Bal, V. Stojevic, F. Pollmann, and A. G. Green, Parallel quantum simulation of large systems on small NISQ computers, *npj Quantum Inf.* **7**, 79 (2021).
- [34] R. Haghshenas, J. Gray, A. C. Potter, and G. K.-L. Chan, Variational power of quantum circuit tensor networks, *Phys. Rev. X* **12**, 011047 (2022).
- [35] J.-G. Liu, Y.-H. Zhang, Y. Wan, and L. Wang, Variational quantum eigensolver with fewer qubits, *Phys. Rev. Research* **1**, 023025 (2019).
- [36] C. D. Batista and G. Ortiz, Algebraic approach to interacting quantum systems, *Adv. Phys.* **53**, 1 (2004).
- [37] L. Isaev, G. Ortiz, and J. Dukelsky, The phase diagram of the Heisenberg antiferromagnet with four-spin interactions, *J. Phys. Condens. Matter* **22**, 016006 (2009).
- [38] L. Isaev, G. Ortiz, and J. Dukelsky, Local physics of magnetization plateaux in the Shastry-Sutherland model, *Phys. Rev. Lett.* **103**, 177201 (2009).
- [39] L. Isaev, G. Ortiz, and J. Dukelsky, Hierarchical mean-field approach to the J_1-J_2 Heisenberg model on a square lattice, *Phys. Rev. B* **79**, 024409 (2009).
- [40] D. Huerga, J. Dukelsky, and G. E. Scuseria, Composite boson mapping for lattice boson systems, *Phys. Rev. Lett.* **111**, 045701 (2013).
- [41] D. Huerga, J. Dukelsky, N. Laflorencie, and G. Ortiz, Chiral phases of two-dimensional hard-core bosons with frustrated ring exchange, *Phys. Rev. B* **89**, 094401 (2014).
- [42] D. Huerga, S. Capponi, J. Dukelsky, and G. Ortiz, Staircase of crystal phases of hard-core bosons on the kagome lattice, *Phys. Rev. B* **94**, 165124 (2016).
- [43] F. Arute, K. Arya, R. Babbush, *et al.*, Quantum supremacy using a programmable superconducting processor, *Nature* **574**, 505 (2019).
- [44] S. Krinner, N. Lacroix, A. Remm, A. D. Paolo, E. Genois, C. Leroux, C. Hellings, S. Lazar, F. Swiadek, J. Herrmann, *et al.*, Realizing repeated quantum error correction in a distance-three surface code (2021), [arXiv:2112.03708 \[quant-ph\]](https://arxiv.org/abs/2112.03708).
- [45] C. Bravo-Prieto, J. Lumbreras-Zarapico, L. Tagliacozzo, and J. I. Latorre, Scaling of variational quantum circuit depth for condensed matter systems, *Quantum* **4**, 272 (2020).
- [46] A. Kandala, A. Mezzacapo, K. Temme, M. Takita, M. Brink, J. M. Chow, and J. M. Gambetta, Hardware-efficient variational quantum eigensolver for small molecules and quantum magnets, *Nature* **549**, 242 (2017).
- [47] P. Chandra and B. Douçot, Possible spin-liquid state at large S for the frustrated square Heisenberg lattice, *Phys. Rev. B* **38**, 9335 (1988).
- [48] E. Dagotto and A. Moreo, Phase diagram of the frustrated spin-1/2 Heisenberg antiferromagnet in 2 dimensions, *Phys. Rev. Lett.* **63**, 2148 (1989).
- [49] R. R. P. Singh and R. Narayanan, Dimer versus twist order in the J_1-J_2 model, *Phys. Rev. Lett.* **65**, 1072 (1990).
- [50] N. Read and S. Sachdev, Large- N expansion for frustrated quantum antiferromagnets, *Phys. Rev. Lett.* **66**, 1773 (1991).
- [51] L. Capriotti and S. Sorella, Spontaneous plaquette dimerization in the J_1-J_2 Heisenberg model, *Phys. Rev. Lett.* **84**, 3173 (2000).
- [52] M. Mambrini, A. Läuchli, D. Poilblanc, and F. Mila, Plaquette valence-bond crystal in the frustrated Heisenberg quantum antiferromagnet on the square lattice, *Phys. Rev. B* **74**, 144422 (2006).
- [53] R. Darradi, O. Derzhko, R. Zinke, J. Schulenburg, S. E. Krüger, and J. Richter, Ground state phases of the spin-1/2 J_1-J_2 Heisenberg antiferromagnet on the square lattice: A high-order coupled cluster treatment, *Phys. Rev. B* **78**, 214415 (2008).
- [54] J. Richter and J. Schulenburg, The spin-1/2 J_1-J_2 Heisenberg antiferromagnet on the square lattice: Exact diagonalization for $N=40$ spins, *EPJ B* **73**, 117 (2010).
- [55] H.-C. Jiang, H. Yao, and L. Balents, Spin liquid ground state of the spin-1/2 square J_1-J_2 Heisenberg model, *Phys. Rev. B* **86**, 024424 (2012).
- [56] J.-F. Yu and Y.-J. Kao, Spin-1/2 J_1-J_2 Heisenberg antiferromagnet on a square lattice: A plaquette renormalized tensor network study, *Phys. Rev. B* **85**, 094407 (2012).
- [57] W.-J. Hu, F. Becca, A. Parola, and S. Sorella, Direct evidence for a gapless Z_2 spin liquid by frustrating Néel antiferromagnetism, *Phys. Rev. B* **88**, 060402 (2013).
- [58] L. Wang, D. Poilblanc, Z.-C. Gu, X.-G. Wen, and F. Verstraete, Constructing a gapless spin-liquid state for the spin-1/2 J_1-J_2 Heisenberg model on a square lattice, *Phys. Rev. Lett.* **111**, 037202 (2013).
- [59] S.-S. Gong, W. Zhu, D. N. Sheng, O. I. Motrunich, and M. P. A. Fisher, Plaquette ordered phase and quantum phase diagram in the spin- $\frac{1}{2}$ J_1-J_2 square Heisenberg model, *Phys. Rev. Lett.* **113**, 027201 (2014).
- [60] S. Morita, R. Kaneko, and M. Imada, Quantum spin liquid in spin 1/2 J_1-J_2 Heisenberg model on square lattice:

- Many-variable variational Monte Carlo study combined with quantum-number projections, *J. Phys. Soc. Japan* **84**, 024720 (2015).
- [61] L. Wang, Z.-C. Gu, F. Verstraete, and X.-G. Wen, Tensor-product state approach to spin-1/2 square J_1 - J_2 antiferromagnetic Heisenberg model: Evidence for deconfined quantum criticality, *Phys. Rev. B* **94**, 075143 (2016).
- [62] L. Wang and A. W. Sandvik, Critical level crossings and gapless spin liquid in the square-lattice spin-1/2 J_1 - J_2 Heisenberg antiferromagnet, *Phys. Rev. Lett.* **121** (2018).
- [63] D. Huerga, A. Greco, C. Gazza, and A. Muramatsu, Translation-invariant parent hamiltonians of valence bond crystals, *Phys. Rev. Lett.* **118**, 167202 (2017).
- [64] G. H. Golub and C. F. Van Loan, *Matrix computations*, 2nd ed., Vol. 3;3.; (Johns Hopkins University Press, Baltimore, Md, 1989).
- [65] J. M. Arrazola, O. D. Matteo, N. Quesada, S. Jahangiri, A. Delgado, and N. Killoran, Universal quantum circuits for quantum chemistry (2021), [arXiv:2106.13839 \[quant-ph\]](https://arxiv.org/abs/2106.13839).
- [66] D. M. Abrams, N. Didier, B. R. Johnson, M. P. d. Silva, and C. A. Ryan, Implementation of xy entangling gates with a single calibrated pulse, *Nat. Electron.* **3**, 744 (2020).
- [67] N. Lacroix, C. Hellings, C. K. Andersen, A. Di Paolo, A. Remm, S. Lazar, S. Krinner, G. J. Norris, M. Gaburac, J. Heinsoo, A. Blais, C. Eichler, and A. Wallraff, Improving the performance of deep quantum optimization algorithms with continuous gate sets, *PRX Quantum* **1**, 110304 (2020).
- [68] D. González-Cuadra, Higher-order topological quantum paramagnets, *Phys. Rev. B* **105**, L020403 (2022).
- [69] N. Trivedi and D. M. Ceperley, Green-function Monte Carlo study of quantum antiferromagnets, *Phys. Rev. B* **40**, 2737 (1989).
- [70] R. H. Byrd, P. Lu, J. Nocedal, and C. Zhu, A limited memory algorithm for bound constrained optimization, *SIAM J. Sci. Comput.* **16**, 1190 (1995).
- [71] C. Zhu, R. H. Byrd, P. Lu, and J. Nocedal, Algorithm 778: L-BFGS-B: Fortran subroutines for large-scale bound-constrained optimization, *ACM Trans. Math. Softw.* **23**, 550 (1997).
- [72] I. L. Markov and Y. Shi, Simulating quantum computation by contracting tensor networks, *SIAM J. Comput.* **38**, 963 (2008).
- [73] Z.-Y. Chen, Q. Zhou, C. Xue, X. Yang, G.-C. Guo, and G.-P. Guo, 64-qubit quantum circuit simulation, *Sci. Bull.* **63**, 964 (2018).
- [74] S. Boixo, S. V. Isakov, V. N. Smelyanskiy, and H. Neven, Simulation of low-depth quantum circuits as complex undirected graphical models (2018), [arXiv:1712.05384 \[quant-ph\]](https://arxiv.org/abs/1712.05384).
- [75] H. De Raedt, F. Jin, D. Willsch, M. Willsch, N. Yoshioka, N. Ito, S. Yuan, and K. Michielsen, Massively parallel quantum computer simulator, eleven years later, *Comput. Phys. Commun.* **237**, 47 (2019).
- [76] C. Monroe, W. Campbell, L.-M. Duan, Z.-X. Gong, A. Gorshkov, P. Hess, R. Islam, K. Kim, N. Linke, G. Pagano, *et al.*, Programmable quantum simulations of spin systems with trapped ions, *Rev. Mod. Phys.* **93** (2021).
- [77] J. Schulenburg, A. Honecker, J. Schnack, J. Richter, and H.-J. Schmidt, Macroscopic magnetization jumps due to independent magnons in frustrated quantum spin lattices, *Phys. Rev. Lett.* **88**, 167207 (2002).
- [78] F. Kobayashi, K. Mitarai, and K. Fujii, Parent Hamiltonian as a benchmark problem for variational quantum eigensolvers (2021), [arXiv:2109.11759 \[quant-ph\]](https://arxiv.org/abs/2109.11759).
- [79] R. Sagastizabal, X. Bonet-Monroig, M. Singh, M. A. Rol, C. C. Bultink, X. Fu, C. H. Price, V. P. Ostroukh, N. Muthusubramanian, A. Bruno, *et al.*, Experimental error mitigation via symmetry verification in a variational quantum eigensolver, *Phys. Rev. A* **100** (2019).
- [80] O. Higgott, D. Wang, and S. Brierley, Variational quantum computation of excited states, *Quantum* **3**, 156 (2019).
- [81] Y. Salathé, M. Mondal, M. Oppliger, J. Heinsoo, P. Kurpiers, A. Potočnik, A. Mezzacapo, U. Las Heras, L. Lamata, E. Solano, S. Filipp, and A. Wallraff, Digital quantum simulation of spin models with circuit quantum electrodynamics, *Phys. Rev. X* **5**, 021027 (2015).
- [82] R. Barends, C. M. Quintana, A. G. Petukhov, Y. Chen, D. Kafri, K. Kechedzhi, R. Collins, O. Naaman, S. Boixo, F. Arute, *et al.*, Diabatic gates for frequency-tunable superconducting qubits, *Phys. Rev. Lett.* **123**, 210501 (2019).
- [83] B. Foxen *et al.* (Google AI Quantum), Demonstrating a continuous set of two-qubit gates for near-term quantum algorithms, *Phys. Rev. Lett.* **125**, 120504 (2020).

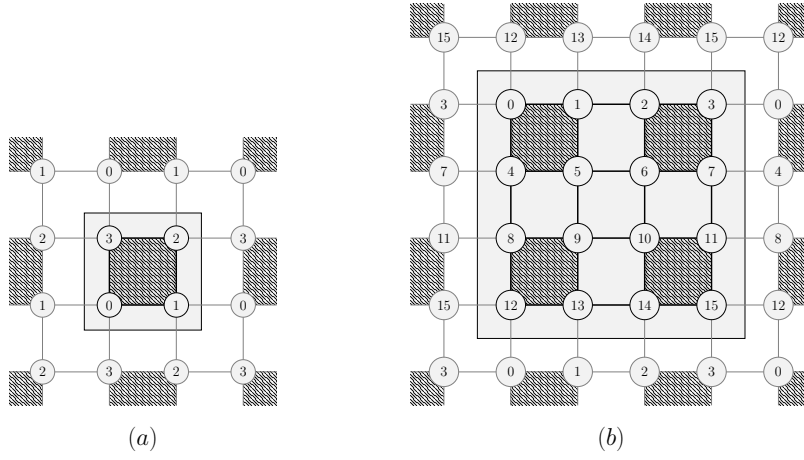


FIG. S1. (a) 2×2 and (b) 4×4 clusters, together with their neighboring sites generating the mean-field embedding. Hatched squares provide a schematic picture of the *plaquette*-VBS order characterized by the dimer observable.

Supplementary Material

2×2 - AND 4×4 - CLUSTER-GUTZWILLER

Given a tiling of the lattice and the cluster-Gutzwiller ansatz, the energy per spin of a translational invariant Hamiltonian reduces to the contribution of the terms acting within the cluster and those connecting different clusters. The variational parameters determining the wave function of the cluster are determined through the Rayleigh-Schrödinger variational principle. When considering a *uniform* ansatz (i.e. translational invariant in the coarsened lattice), such energy minimization reduces to minimizing the energy of a single cluster in a self-consistent mean-field embedding. For the specific case of the 2×2 cluster used in this work, the energy per spin of the J_1 - J_2 Hamiltonian is

$$E(\boldsymbol{\theta}) = \frac{1}{4} [J_1 (\langle \mathbf{S}_0 \mathbf{S}_1 \rangle + \langle \mathbf{S}_1 \mathbf{S}_2 \rangle + \langle \mathbf{S}_2 \mathbf{S}_3 \rangle + \langle \mathbf{S}_3 \mathbf{S}_0 \rangle) + J_2 (\langle \mathbf{S}_0 \mathbf{S}_2 \rangle + \langle \mathbf{S}_1 \mathbf{S}_3 \rangle) + J_1 (\langle \mathbf{S}_0 \rangle \langle \mathbf{S}_1 \rangle + \langle \mathbf{S}_1 \rangle \langle \mathbf{S}_2 \rangle + \langle \mathbf{S}_2 \rangle \langle \mathbf{S}_3 \rangle + \langle \mathbf{S}_3 \rangle \langle \mathbf{S}_0 \rangle) + 3J_2 (\langle \mathbf{S}_0 \rangle \langle \mathbf{S}_2 \rangle + \langle \mathbf{S}_1 \rangle \langle \mathbf{S}_3 \rangle)], \quad (\text{S1})$$

where all expectation values are taken with respect to the wave function of the cluster $|\psi(\boldsymbol{\theta})\rangle$. Equivalently, the energy per spin obtained with the 4×4 cluster-Gutzwiller ansatz,

$$E(\boldsymbol{\theta}) = \frac{1}{16} [J_1 \sum_{\langle i,j \rangle \in \square} \langle \mathbf{S}_i \mathbf{S}_j \rangle + J_2 \sum_{\langle\langle i,j \rangle\rangle \in \square} \langle \mathbf{S}_i \mathbf{S}_j \rangle + J_1 (\langle \mathbf{S}_0 \rangle \langle \mathbf{S}_{12} \rangle + \langle \mathbf{S}_1 \rangle \langle \mathbf{S}_{13} \rangle + \langle \mathbf{S}_2 \rangle \langle \mathbf{S}_{14} \rangle + \langle \mathbf{S}_3 \rangle \langle \mathbf{S}_{15} \rangle + \langle \mathbf{S}_3 \rangle \langle \mathbf{S}_0 \rangle + \langle \mathbf{S}_7 \rangle \langle \mathbf{S}_4 \rangle + \langle \mathbf{S}_{11} \rangle \langle \mathbf{S}_8 \rangle + \langle \mathbf{S}_{15} \rangle \langle \mathbf{S}_{12} \rangle) + J_2 (\langle \mathbf{S}_0 \rangle \langle \mathbf{S}_{13} \rangle + \langle \mathbf{S}_1 \rangle \langle \mathbf{S}_{12} \rangle + \langle \mathbf{S}_1 \rangle \langle \mathbf{S}_{14} \rangle + \langle \mathbf{S}_2 \rangle \langle \mathbf{S}_{13} \rangle + \langle \mathbf{S}_2 \rangle \langle \mathbf{S}_{15} \rangle + \langle \mathbf{S}_3 \rangle \langle \mathbf{S}_{14} \rangle + \langle \mathbf{S}_3 \rangle \langle \mathbf{S}_{12} \rangle + \langle \mathbf{S}_0 \rangle \langle \mathbf{S}_{15} \rangle + \langle \mathbf{S}_3 \rangle \langle \mathbf{S}_4 \rangle + \langle \mathbf{S}_7 \rangle \langle \mathbf{S}_0 \rangle + \langle \mathbf{S}_7 \rangle \langle \mathbf{S}_8 \rangle + \langle \mathbf{S}_{11} \rangle \langle \mathbf{S}_4 \rangle + \langle \mathbf{S}_{11} \rangle \langle \mathbf{S}_{12} \rangle + \langle \mathbf{S}_{15} \rangle \langle \mathbf{S}_8 \rangle)]. \quad (\text{S2})$$

If the parameterization of the wave function is lineal, i.e. $|\psi(\boldsymbol{\theta})\rangle = \sum \theta_{\{S_j^z\}} |\{S_j^z\}\rangle$ with $\theta \in \mathbb{C}$ uncovers the whole Hilbert space of the cluster, equating the derivative of the energy to zero, $\partial_{\theta_k} E(\boldsymbol{\theta}) = 0$, leads to a non-linear set of equations that can be cast in matrix form, and solved by iteratively performing exact diagonalization of the $L \times L$ cluster with open boundary conditions and a set of self-consistent mean-fields, $\langle \psi(\boldsymbol{\theta}) | \mathbf{S}_j | \psi(\boldsymbol{\theta}) \rangle$, acting on its boundaries. Restriction to the null magnetization subspace, $\sum_{j \in \square} \langle S_j^z \rangle = 0$, restricts the onset of magnetizations along z , i.e. $\langle S_j^{x,y} \rangle = 0$, and allows to increase the efficiency of the computation while still allowing for the eventual breakdown of SU(2) and onset of long-range order (LRO). Nevertheless, exact diagonalization is limited by classical computing resources to $N \lesssim 30$.

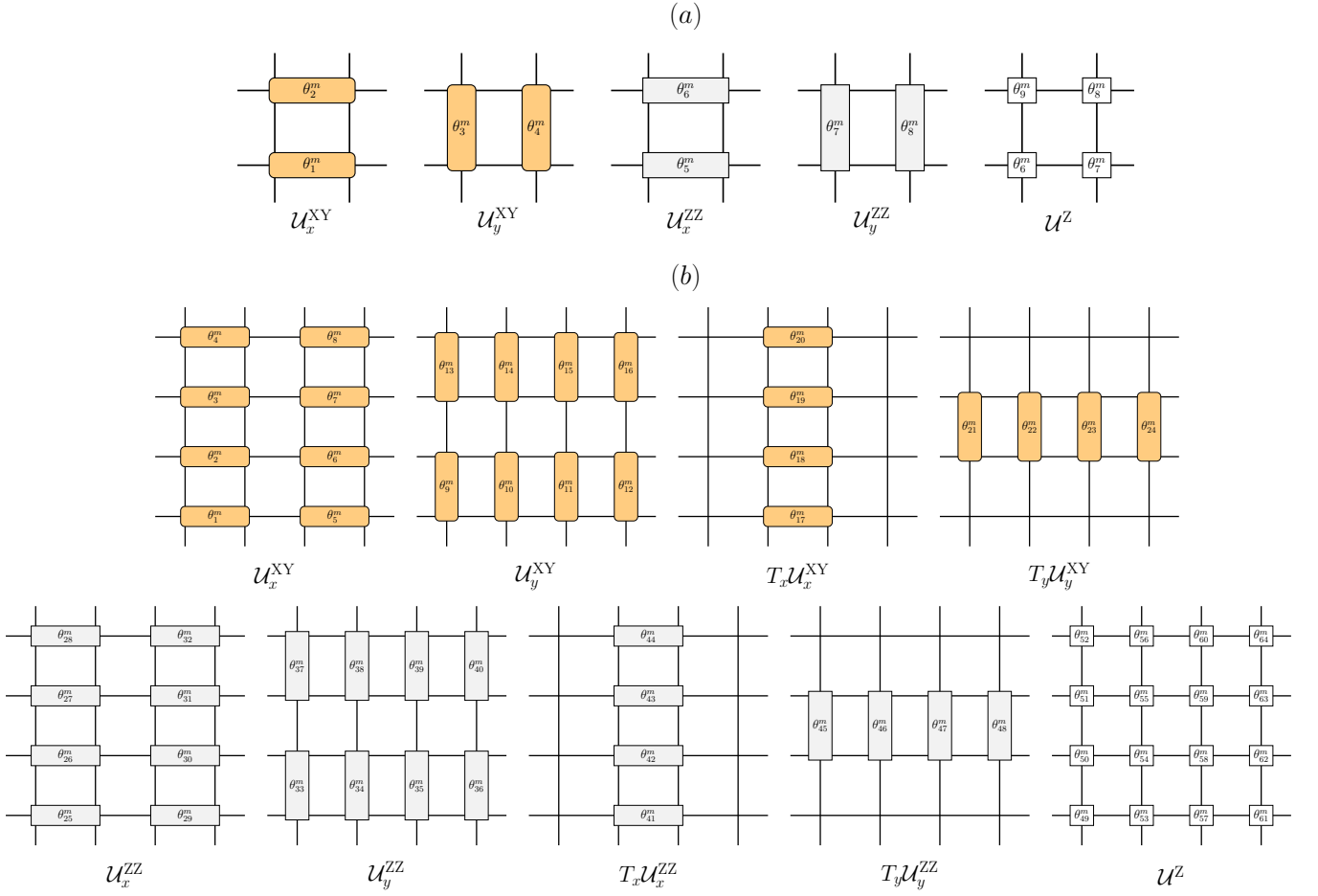


FIG. S2. Ordered set of layers of REAL-XY gates (orange rounded rectangles), ZZ- (gray rectangles), and Z-rotations (white squares) comprising a *macro-layer* of the PQC for (a) 2×2 and (b) 4×4 clusters, where θ_k^m labels the k th variational parameter within the m th macro-layer. Generalization to even $L \times L > 4 \times 4$ is straightforward and has the same depth as $L=4$, $d=9m$.

U(1) PARAMETERIZED QUANTUM CIRCUITS

As described in the main text, the PQC is constructed by a recursive application of two-qubit XY gates respecting nearest-neighbor (NN) connectivities in an order that minimizes the circuit depth and respects the C_4 symmetry as much as possible, and additional ZZ- and Z-rotation gates, as shown in Fig. (S2) for 2×2 and 4×4 clusters. Such a XY-ZZ-Z macro-layer structure is repeated m times to gain numerical accuracy.

As few as $m=2$ macro-layers are sufficient to provide with a good approximation to the classical cluster-Gutzwiller results, which consider a cluster wave function uncovering the whole Hilbert space of the cluster. In particular, for 2×2 the hybrid Q-HMFT converges exactly to the classical cluster-Gutzwiller results with $m=2$ and same parameter within the XY and ZZ layers, respectively, i.e. $\theta_1^m = \theta_2^m = \theta_3^m = \theta_4^m$ and $\theta_5^m = \theta_6^m = \theta_7^m = \theta_8^m$, where we have defined θ_k^m as the k th parameter within the macro-layer m .

In view of the numerical results presented for 4×4 clusters, we conjecture that the classical cluster-Gutzwiller solution is recovered for $m \rightarrow \infty$ for general L .